Numerical Simulation of Mammatus

KATHARINE M. KANAK*

Cooperative Institute for Mesoscale Meteorological Studies, University of Oklahoma, Norman, Oklahoma

JERRY M. STRAKA

School of Meteorology, University of Oklahoma, Norman, Oklahoma

DAVID M. SCHULTZ

Division of Atmospheric Sciences, Department of Physical Sciences, University of Finland, and Finnish Meteorological Institute, Helsinki, Finland

(Manuscript received 19 March 2007, in final form 6 September 2007)

ABSTRACT

Mammatus are hanging lobes on the underside of clouds. Although many different mechanisms have been proposed for their formation, none have been rigorously tested. In this study, three-dimensional numerical simulations of mammatus on a portion of a cumulonimbus cirruslike anvil are performed to explore some of the dynamic and microphysical factors that affect mammatus formation and evolution. Initial conditions for the simulations are derived from observed thermodynamic soundings. Five observed soundings are chosen—four were associated with visually observed mammatus and one was not. Initial microphysical conditions in the simulations are consistent with in situ observations of cumulonimbus anvil and mammatus. Mammatus form in the four model simulations initialized with the soundings for which mammatus were observed, whereas mammatus do not form in the model simulation initialized with the no-mammatus sounding. Characteristics of the modeled mammatus compare favorably to previously published mammatus observations.

Three hypothesized formation mechanisms for mammatus are tested: cloud-base detrainment instability, fallout of hydrometeors from cloud base, and sublimation of ice hydrometeors below cloud base. For the parameters considered, cloud-base detrainment instability is a necessary, but not sufficient, condition for mammatus formation. Mammatus can form without fallout, but not without sublimation. All the observed soundings for which mammatus were observed feature a dry-adiabatic subcloud layer of varying depth with low relative humidity, which supports the importance of sublimation to mammatus formation.

1. Introduction

Mammatus are hanging lobes on the underside of clouds, typically cumulonimbus anvils, although many other parent cloud types have been observed (e.g., Glickman 2000; Schultz et al. 2006). Despite mammatus being some of the most photographed and aesthetically pleasing cloud forms, relatively little is known about the environment, origin, structure, size, microphysical properties, and dynamics of mammatus. A comprehensive review of observations and proposed formation mechanisms appears in Schultz et al. (2006), who documented ten different proposed formation mechanisms. Because observations of mammatus are often limited to those taken from just one type of observing system and do not include all the thermodynamic, moisture, and dynamic measurements complete in space and time, rigorous evaluation of these proposed mechanisms is difficult. Thus, numerical simulations provide an attractive methodology to evaluate some of these proposed formation mechanisms.

The purpose of this work is to numerically evaluate several of the proposed formation mechanisms using idealized numerical simulations of cirrus anvils of cu-

* Current affiliation: School of Meteorology, University of Oklahoma, Norman, Oklahoma.

Corresponding author address: Dr. Jerry M. Straka, 120 David L. Boren Blvd., Suite 5900, Norman, OK 73072-7304.
E-mail: jmstraka@cox.net

DOI: 10.1175/2007JAS2469.1

mulonimbus clouds. The model domain consists of a portion of the anvil, and the simulations are initialized with observed soundings from environments characterized by anvils with and without mammatus observed on their underside. The simulations in this study build upon Kanak and Straka (2006), who explicitly simulated mammatus in a simulation initialized with a sounding from an observed case of mammatus associated with a cumulonimbus anvil over Norman, Oklahoma, on 20 May 2001. Sets of model experiments allow systematic evaluation of several of the proposed mechanisms. In addition, the sensitivity of the modeled mammatus to changes in the ambient environment can be examined.

Section 2 of this paper is a description of the numerical model, the design of the numerical experiments, and the observed soundings used to initialize the model simulations. The model simulation results are presented in section 3. Evidence suggests that subcloud sublimation of hydrometeors is responsible for the mammatus. This hypothesis is tested in section 4 as part of an evaluation of three different mammatus formation mechanisms: cloud-base detrainment instability (CDI), hydrometeor fallout, and sublimation. Further experiments are performed in section 5 to determine the sensitivity of the formation and size of mammatus to the subcloud static stability and subcloud relative humidity. Section 6 contains the conclusions of the paper.

2. Methodology

The numerical model, the Straka Atmospheric Model, is described in section 2a, followed by the design of the numerical experiments and the formulation of the initial conditions in section 2b. The base-state initial conditions for the simulations derive from observed thermodynamic soundings: four soundings were associated with observed mammatus and one was not. These initial conditions are presented in section 2c.

a. Numerical model description

The Straka Atmospheric Model is a three-dimensional, fully compressible, nonhydrostatic model; the model equations are presented in Carpenter et al. (1998) and are cast on an Arakawa C-grid. Divergence and pressure gradient are solved using sixth-order centered spatial differences. The velocity fields are advected with a sixth-order local spectral scheme (Straka and Anderson 1993), whereas the scalars are advected with a sixth-order Crowley flux scheme (Tremback et al. 1987) with a flux limiter (Leonard 1991). The subgrid turbulence closure is a 1.5-order scheme (Deardorff 1980) using sixth-order numerics. Integrations of the fast- and slow-solution modes are split from each other, with the centered-in-time leapfrog scheme used for the slow modes and an explicit forward–backward solver for the pressure gradient in the velocity equations and mass flux divergence in the pressure equation. Shortwave and longwave radiation processes that may be formation mechanisms for mammatus (e.g., section 3f in Schultz et al. 2006) are not considered for this particular study.

TABLE 1. Summary of numerical experiment names, dates of observed soundings used to initialize the simulations, and description of the simulations.

Expt	Date	Description
M1	0000 UTC 19 Sep 2002	Mammatus
M2	0000 UTC 21 May 2001	Mammatus
M3	0000 UTC 1 Sep 2001	Mammatus
M4	0000 UTC 25 May 2004	Mammatus
N1	1200 UTC 8 Apr 2004	No mammatus
M2-NOSUBL	0000 UTC 21 May 2001	No sublimation
M2-NOFALL	0000 UTC 21 May 2001	No fallout
STAB0	Idealized	Γ_d
STAB1	Idealized	Lapse rate $+1°C\ km^{-1}$
STAB2	Idealized	Lapse rate $+2°C\ km^{-1}$
STAB3	Idealized	Lapse rate $+3°C\ km^{-1}$
RH10	Idealized	10% RH
RH30	Idealized	30% RH
RH50	Idealized	50% RH
RH70	Idealized	70% RH
RH90	Idealized	90% RH

The microphysical processes in the model are described by Straka and Mansell (2005). Ice crystal mixing ratios and snow aggregate mixing ratios are specified in the initial cloud using an inverse exponential distribution in size; more information on the initialization of the cloud microphysical fields is given in section 2b. The microphysical processes represented in these simulations include sublimation and deposition of ice crystals and snow aggregates, along with aggregation of ice crystals into snow aggregates. As there is no available cloud water in the model domain, riming (hence, the formation of rimed ice crystals, rimed snow aggregates, graupel, and other large ice particles) does not occur.

b. Numerical experiment design

Table 1 shows a summary of the numerical experiments that were performed. The model domain is intended to represent a portion of a cumulonimbus anvil at some distance downwind of the main cumulonimbus updraft to be consistent with observations. For example, Stith (1995, his Fig. 1b) reported mammatus lo-

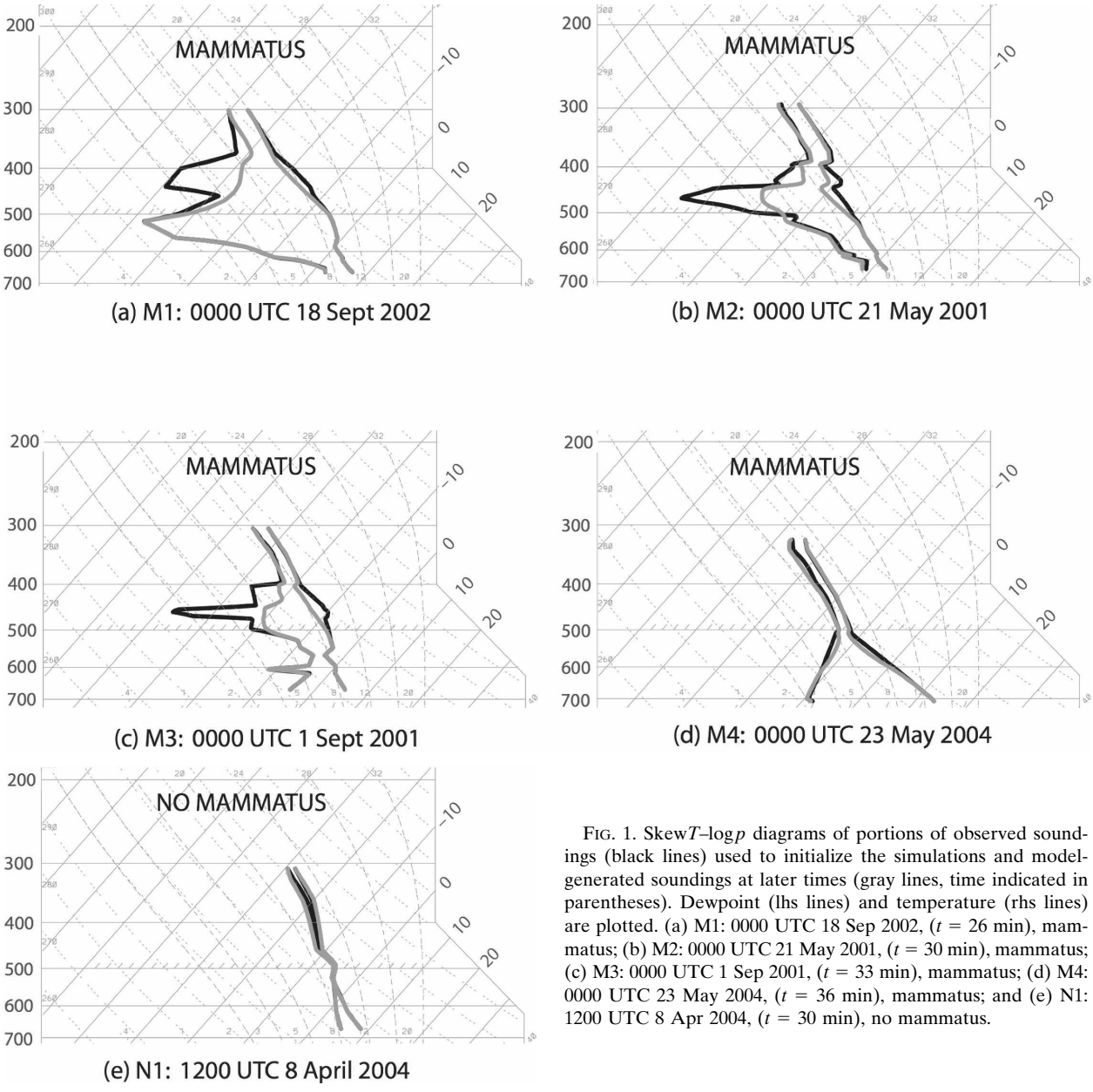

FIG. 1. Skew$T$–log$p$ diagrams of portions of observed soundings (black lines) used to initialize the simulations and model-generated soundings at later times (gray lines, time indicated in parentheses). Dewpoint (lhs lines) and temperature (rhs lines) are plotted. (a) M1: 0000 UTC 18 Sep 2002, (t = 26 min), mammatus; (b) M2: 0000 UTC 21 May 2001, (t = 30 min), mammatus; (c) M3: 0000 UTC 1 Sep 2001, (t = 33 min), mammatus; (d) M4: 0000 UTC 23 May 2004, (t = 36 min), mammatus; and (e) N1: 1200 UTC 8 Apr 2004, (t = 30 min), no mammatus.

cated 70 km from the main updraft. The model domain is 4000 m $\times$ 4000 m $\times$ 6000 m with 50-m grid spacing in all three Cartesian directions (80 $\times$ 80 $\times$ 120 grid points). The domain extends from 3500 to 9500 m above ground level (AGL) in all but one simulation (M4, see Table 1) in which the domain extends from 3000 to 9000 m AGL to better position the anvil in the model domain. At the upper and lower boundaries, the vertical velocity is zero and the boundaries are free slip. The lateral boundary conditions are periodic. A model time step of 1 s is used for the slow modes and a small time step of 0.04 s is used for the explicitly integrated fast modes to ensure numerical stability.

The initial thermodynamics and velocity conditions are horizontally homogeneous, and base-state temperature and dewpoint profiles are specified using observed sounding data, shown in Fig. 1 and discussed in section 2c. No mean winds are prescribed in these simulations, which eliminates from consideration proposed mammatus mechanisms related to vertical shear of the horizontal wind (section 3h in Schultz et al. 2006).

Consistent with characteristics of cirrus observations by Heymsfield and Knollenberg (1972) and Stith (1995), the model is initialized by specifying a constant ice crystal mixing ratio of 1.00×10^{-3} kg kg^{-1} between 8500 and 9500 m. Then, random perturbations of ice

crystal mixing ratio of $\pm 0.25 \times 10^{-3}$ kg kg^{-1} are added at the initial time step in this layer. In addition, a snow aggregate mixing ratio of 0.75×10^{-3} kg kg^{-1} is specified in the same layer with random perturbations of $\pm 0.25 \times 10^{-3}$ kg kg^{-1}. These perturbations to the initial microphysical fields are necessary to produce spatial inhomogeneities that result in vertical motions. (In addition, perturbations in both temperature and wind components were tested and, for the amplitudes of perturbations used, mammatus did not form. Although the perturbations may not have been strong enough, the initial cloud-layer stability likely damped these perturbations.) Model test simulations without initial random ice crystal and snow aggregate perturbations did not produce mammatus. Although it is not known if the magnitude of the ice crystal and snow aggregate mixing perturbations is reasonable for the generation of mammatus, the mixing ratio of snow aggregates generated by this cloud ice field is physically plausible for cirrus anvils [e.g., when compared to observations in Heymsfield (1986)].

When only ice crystals (no snow aggregates) are initialized in the simulations, mammatus form, although at an initially slower rate. Once snow aggregates form from just ice crystals, the rate of growth of ice crystals and snow aggregates is very similar to those simulations employing only snow aggregates in the initial conditions. Thus, the model simulations are somewhat robust to the specification of the initial microphysical conditions.

c. *Observed soundings used to initialize model*

All of the soundings used to initialize the model simulations were taken from Norman. Mammatus at, or near, the time of the sounding release for soundings used to initialize simulations M1–M4 (Figs. 1a–d) were visually observed by one or more of the coauthors from locations within about 5 km of the sounding release point. For case M1 (Fig. 1a), mammatus were observed from 2330 UTC 18 September to 0030 UTC 19 September 2002. For case M2 (Fig. 1b), the case used for the simulation in Kanak and Straka (2006), mammatus were observed at 2351 UTC 20 May 2001. For case M3 (Fig. 1c), the exact time of the visual observation of mammatus on the evening of 1 September 2001 was not recorded. For case M4 (Fig. 1d), mammatus were observed from about 2310 UTC 23 May to 0000 UTC 24 May 2004. For case N1 (Fig. 1e), anvil cloud was present at the time of the sounding launch (about 1100 UTC 8 April 2004), but mammatus were not visually observed.

The soundings for M1–M4 (Figs. 1a–d) showed some similarities, specifically the moist, near-saturated, cloud layer above a dry, low-stability (dry adiabatic) layer at least 50–100 hPa deep. These proximity soundings with the dry subcloud layer are similar to some mammatus proximity soundings presented in the literature (e.g., Clarke 1962; Fig. 7 in Winstead et al. 2001; Fig. 10 in Schultz et al. 2006), although they differ from others that have a more moist subcloud layer (e.g., Fig. 8 in Stith 1995; Fig. 1 in Martner 1995). The cloud-base temperature is colder than -10°C for all four soundings with most about -20°C or colder (Figs. 1a–d), which indicates that these mammatus likely comprise the ice phase.

Some of the main differences between the soundings M1–M4 include the depth of the subcloud dry layer and the existence of an inversion at anvil base (Figs. 1a–d). The effect of the subcloud dry layer on formation and structure of the mammatus is explored in section 5. The presence of an inversion at the anvil base in Fig. 1b is consistent with some other soundings associated with mammatus (e.g., Clayton 1911; Hartmann 1920; Schneider 1920; Clarke 1962; Stith 1995; Winstead et al. 2001; Schultz et al. 2006).

Although there is some variability in the structure of these mammatus soundings, they differ dramatically from the "no-mammatus" sounding N1 (Fig. 1e), which features much more moist subcloud air. This critical difference in the subcloud relative humidity provides support for proposed mechanisms for mammatus that include subcloud sublimation of ice hydrometeors from the anvil, which is a mechanism tested in section 4.

3. Results of simulations

To represent the visual boundaries of mammatus that closely represent what a human observer might see from the ground, mean snow aggregate diameter (hereafter, simply snow aggregate diameter) is plotted because it is related to cloud opacity and visibility. That is, it is assumed that the size of the particles is proportional to the visibility. The three-dimensional isosurface of 1×10^{-5} m snow aggregate diameter is shown at 30 min into the M2 simulation when the mammatus lobes are mature (Fig. 2). The mammatus lobes cover the entire horizontal dimensions of the model domain, appear cellular, and do not appear to have any linear organization. All model simulations M1–M5 are performed for a total of 40 min. In M1–M4, after about 15–20 min, the descending layers of hydrometeors begin to develop undulations on the lower cloud surface. By 30 min, these undulations have grown into fully developed mammatus lobes (M2; e.g., Fig. 2).

To better visualize the structure of the mammatus lobes, vertical cross sections of the snow aggregate di-

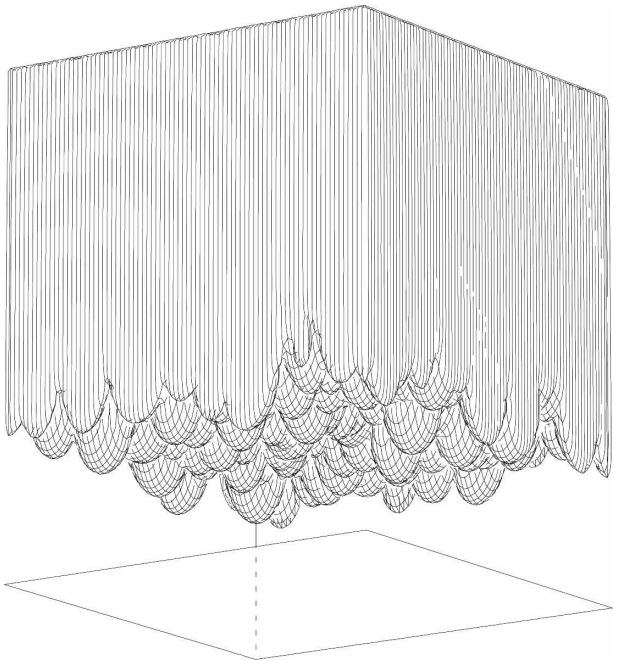

FIG. 2. Three-dimensional isosurface of 1×10^{-5} m mean snow aggregate diameter from M2 at 30 min (looking upward).

ameter through the domain minimum in vertical velocity (that always occurs within a mammatus lobe) are constructed (Fig. 3). The horizontal diameter of the lobes in M2 (Fig. 3a) is about 300–450 m, which is among the smaller observed mammatus sizes in the literature (e.g., Table 2). Vertical motion within the simulated lobes ranges from about -1 m s^{-1} to its minimum value of -7.6 m s^{-1}, which is larger in magnitude than previous measurements (Table 2). Such differences in scale and vertical motion may be due to the inability of the observing instruments to resolve finescale structure represented in the simulations. Circulation within mammatus lobes is similar to the pattern shown by Winstead et al. (2001, their Fig. 6a), with upward return flow around the mammatus lobes labeled 1 and 3 in Fig. 3b. Horizontal rotors exist above some of the lobes (e.g., above lobe 2 in Fig. 3b). There are also some localized extrema in snow aggregate diameter within the lower part of the lobes (e.g., lobe 2 in Fig. 3b). Mammatus similar to those in M2 also form within experiments M1 and M4 (not shown), which are both initialized with soundings possessing deep, well-mixed, subcloud dry air (Figs. 1a,d).

Case M3 (Figs. 3c,d) exhibits mammatus lobes at 33 min that are much narrower (250 m) in diameter and weaker in minimum vertical velocity (-0.61 m s^{-1}) than in M2 (Figs. 3a,b). Furthermore, the vertical gradient of snow aggregate diameter at the base of each mammatus lobe is weaker in M3 than that in M2 (cf. Figs. 3d,b), which may be a result of the more moist subcloud air in M3. Thus, the vertical scale and magnitude of the subcloud dry air may affect the horizontal and vertical scales and microphysical structure of the mammatus.

a. Relative temperatures inside mammatus

One of the important questions regarding mammatus is whether cooling by evaporation or sublimation is responsible for their formation. For example, decreasing particle sizes near the bottom of mammatus lobes inferred from radar observations suggest that sublimation/evaporation is occurring within the lobes (e.g., Martner 1995; Kollias et al. 2005; Wang and Sassen 2006; Schultz et al. 2006). In contrast, Stith's (1995) aircraft penetration of a mammatus lobe showing that the inside of the lobe was 0.7°C warmer inside than outside led him to question whether sublimation was important. To our knowledge, his aircraft penetration is the only in situ evidence of the relative temperature inside mammatus.

To address this question in the simulations, the potential temperature perturbations from the base state are examined for simulations M2 and M3 (Fig. 4). Whether or not the center of a mammatus lobe is warmer or colder than ambient depends on the individual lobes and the height at which the temperature is examined. For example, lobes simulated in M2 have both warmer and colder cores than ambient (Fig. 4a). Specifically, lobe 1 has a warmer-than-ambient core near the bottom of the lobe, whereas lobes 2 and 3 have colder-than-ambient and near-ambient cores (Fig. 4a). Furthermore, lobe 1 is warmer than ambient at lower heights near the base of the lobe; at higher heights, the perturbation is colder than ambient. In contrast, lobes simulated in M3 have core temperatures near ambient for most of the depth of the mammatus lobe (Fig. 4b). The lobes also have different temperature structures with time. For example, lobe 1 in M2 was the same temperature as ambient as much as 4 min prior to the time shown in Fig. 4a before becoming warmer than its environment at the base of the lobe at the time of Fig. 4a. The differences in these temperature perturbations between different simulations may have to do with the phase in the life cycle of the mammatus, the time in the simulation, and the environmental temperature profile.

b. Dissipation of the mammatus field

The behavior of the mammatus lobes late in the simulations varies greatly. For example, at 36 min into the M1 simulation (Fig. 5a), the flow is quite turbulent

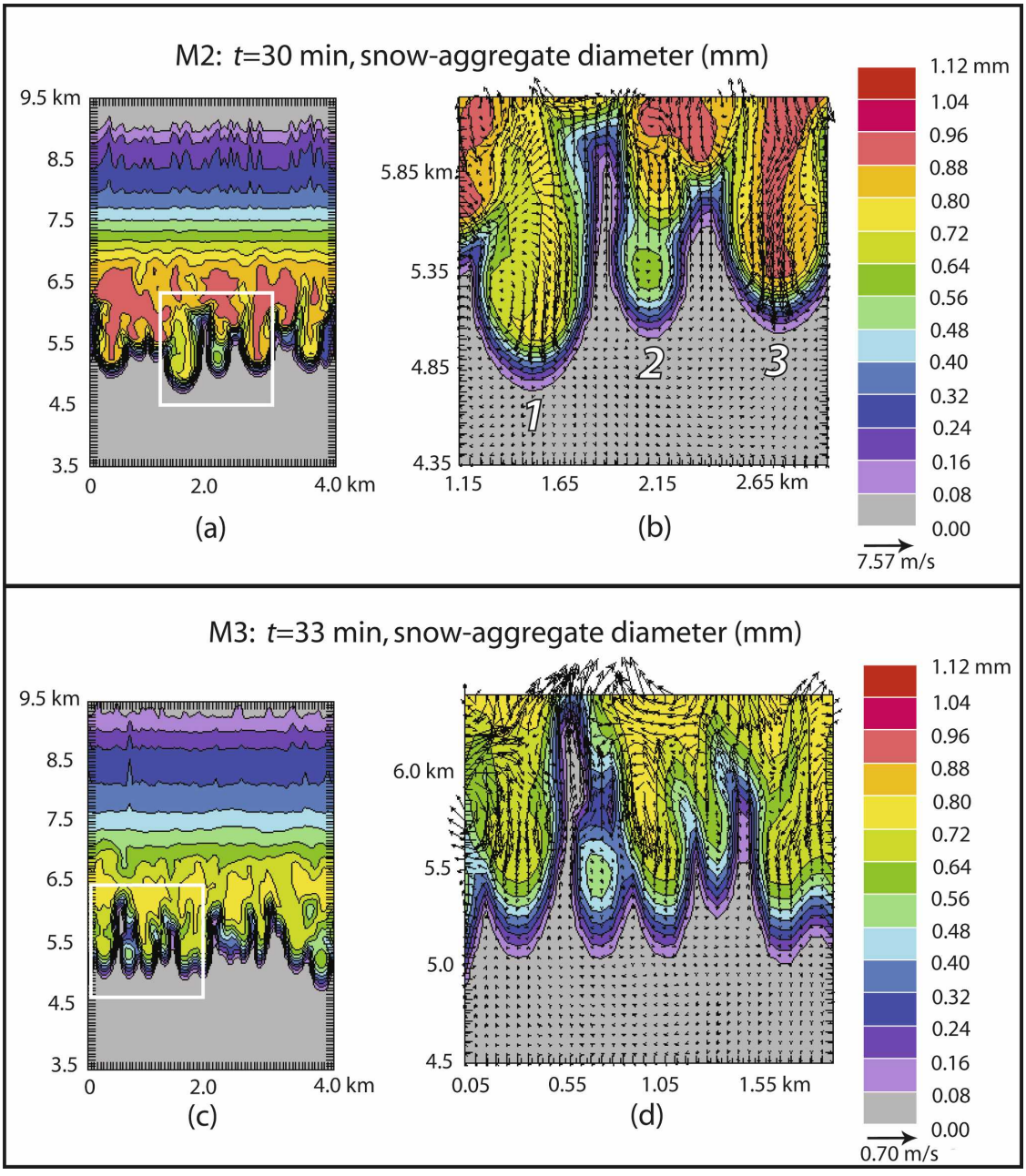

FIG. 3. Vertical cross sections of snow aggregate diameter (mm, color contours). (a) M2: whole domain at $t = 30$ min and $y = 75$ m. (b) M2: inset with velocity vectors. White box in (a) indicates inset in (b). The longest vector corresponds to a wind speed of 7.57 m s^{-1}. Large white numbers represent individual mammatus lobes described in text. (c) M3: whole domain at $t = 33$ min and $y = 1625$ m. (d) M3: inset with velocity vectors. White box in (c) indicates inset in (d). The longest vector corresponds to a wind speed of 0.70 m s^{-1}.

[similar to the observations of turbulent mammatus in Sassen et al.'s (2001) Fig. 8], and the cloud field is retreating upward owing to a lack of sublimating hydrometeors, thus limiting the continued descent of the mammatus. Therefore, this case is an example of limited development of mammatus owing to the amount of initial ice crystal and snow aggregate mixing ratios and the relative humidity of the ambient sounding.

A second possible scenario occurs at 37 min into the M3 simulation (Fig. 5b). The interesting feature is the portion of the mammatus lobe A that has broken away from the lower cloud base. Such behavior resembles the

TABLE 2. Some examples of observed physical characteristics of mammatus.

Study	Vertical velocity ($m\ s^{-1}$)	Horizontal extent (km)
Clarke (1962)	Not observed	0.25–0.75
Warner (1973)	−3.1 to −1.2	0.1–1
Martner (1995)	−3.0 to +0.5	1.1
Stith (1995)	−2.5 to +1.0	2–3
Winstead et al. (2001)	−3 to −2	1–3
Wang and Sassen (2006)	−2 to +0.5	3–7
Kollias et al. (2005)	−6 to +1.5	1–3
Schultz et al. (2006)	−3.5 to 0.0	0.5–2

schematic Fig. 3 in Emanuel (1981) as cloud-base detrainment mixes cloudy air with dry subcloud air. To our knowledge, however, this process in which portions of mammatus lobes break away from the cloud base has not been observed either visually or via remote sensing instrumentation. However, such a process might not be possible to observe from the ground or may appear quite differently when viewed from the ground.

c. *Modification of soundings by mammatus*

The modification of the initial soundings (Fig. 1) by the development of the mammatus may provide insights into the relevant physical processes. In all cases where mammatus form (Figs. 1a–d), the subcloud layers cool and moisten after the descent of the mammatus layer, which is consistent with the results of Kanak and Straka (2006) who showed that sublimation of the ice hydrometeors is responsible for the cooling and moistening in the subcloud layer. In cases M2, M3, and M4, an inversion forms at cloud base at the top of the cooling region as it joins cloud base (Figs. 1b–d). This observation is consistent with previous literature describing cloud-base inversions (Clayton 1911; Hartmann 1920; Schneider 1920; Clarke 1962; Stith 1995; Winstead et al. 2001; Schultz et al. 2006). In M4, a superadiabatic layer also forms around 600 hPa at the base of the greatest cooling, which is a feature also observed in some previous soundings (Fig. 2 in Berg 1938; Fig. 10 in Schultz et al. 2006). Thus, the modification of the atmospheric profiles by the mammatus provides support and a physical explanation for the seemingly contradictory observations of subcloud stable layers and subcloud superadiabatic layers.

4. Tests of proposed mammatus formation mechanisms

In this section, three proposed mammatus formation mechanisms are tested: cloud-base detrainment instability in section 4a, hydrometeor fallout in section 4b, and sublimation in section 4c.

a. *Cloud-base detrainment instability criterion*

One proposed formation mechanism for mammatus is based on mixing similarity theory and is called cloud-base detrainment instability (Emanuel 1981, 1994, 220–221). This theory has its origins from cloud-top entrainment instability except it is applied as detrainment at cloud base. The criterion for CDI is that the liquid-

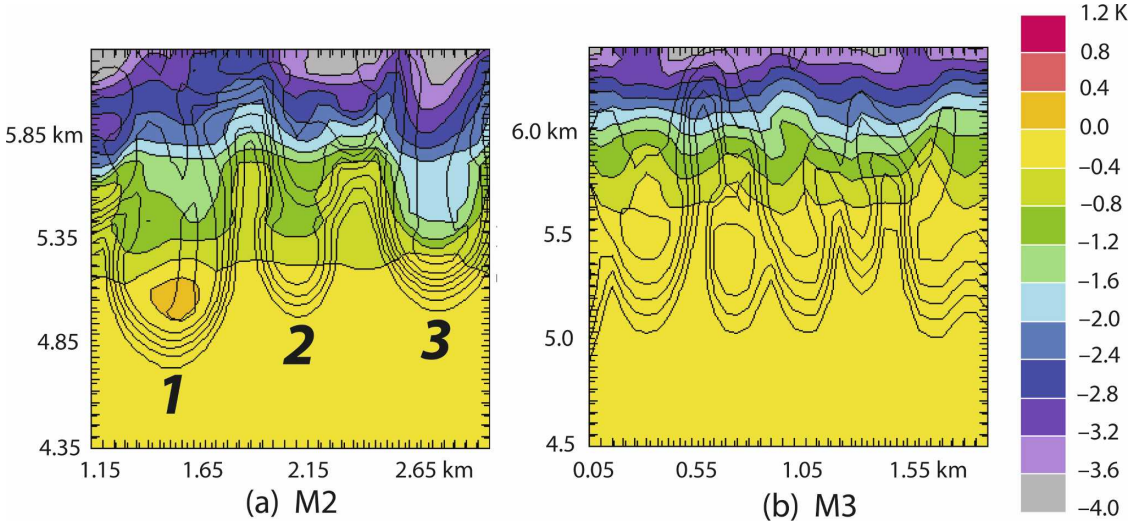

FIG. 4. Vertical cross sections of potential temperature perturbation from the horizontal mean potential temperature (K, color contours) and snow aggregate diameter (mm, black contours). (a) M2 at t = 30 min and y = 75 m. Large black numbers represent individual mammatus lobes described in text. (b) M3 at t = 33 min and y = 1625 m.

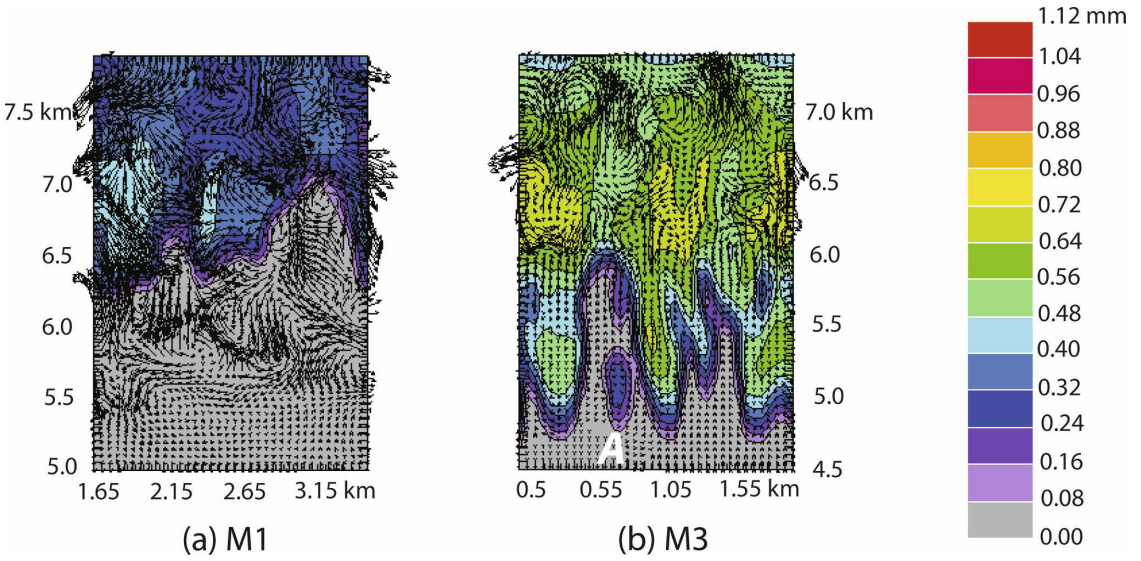

FIG. 5. Vertical cross sections of snow aggregate diameter (mm, color contours) and velocity vectors (black arrows): (a) M1 at $t = 36$ min and $y = 125$ m (the longest vector corresponds to a wind speed of 1.11 m s^{-1}) and (b) M3 at $t = 37$ min and $y = 1625$ m (the longest vector corresponds to a wind speed of 1.74 m s^{-1}). White "A" identifies the detached mammatus lobe described in the text.

water or ice-water static energy of potentially warm, dry subcloud air is higher than that of the cloudy air above.

For liquid processes, Emanuel (1981) presents the CDI criterion as

$$\Delta h_l < 0, \tag{1}$$

where h_l is the liquid static energy and delta is an incremental increase in height across the clear/cloudy interface. The criterion for CDI typically is satisfied when potentially warm, dry air is advected beneath potentially cool, saturated air (Emanuel 1981). This situation is often found beneath cumulonimbus anvils, as well as various other cloud types.

If the CDI criterion is met along an interface between cloudy air above and clear air below, then spontaneous mixing of the moist air downward releases the instability. First, any descended cloudy air is suddenly in an environment ripe for evaporation or sublimation. If the subcloud air is warm and dry enough, all of the hydrometeors may evaporate or sublime if they are liquid or ice, respectively. The air parcel that mixed downward becomes negatively buoyant and descends. Emanuel (1981) argues that this process is most effective if the subcloud layer is of moderate relative humidity. If the subcloud air is too cool, too humid, or both, evaporation/sublimation may be too slow to overcome the adiabatic warming of the descending parcel. If the subcloud air is too warm, too dry, or both, evaporation/sublimation occurs too quickly, allowing only shallow penetration for typical amounts of cloud-ice and snow aggregate mass found in anvils. After the release of the instability, an inversion forms at cloud base and a neutral layer forms below the inversion, which is consistent with the observations and numerical simulations discussed in section 3c.

To evaluate the CDI criterion for the ice clouds simulated in the present study, the expression for θ_{iv} is used (K. Emanuel 2006, personal communication):

$$\theta_{iv} = T_v\left(\frac{p_o}{p}\right)^{\chi}\left(1 - \frac{q_i}{1+q_t}\right)\left(1 - \frac{q_i}{0.622 + q_t}\right)^{\chi-1} \times \left(1 - \frac{q_i}{q_t}\right)^{-\gamma} \exp\left[\frac{-L_s q_i}{(c_p + q_t c_{pv})T}\right], \tag{2}$$

where

$$\chi \equiv \left(\frac{R_d + R_v q_t}{c_p + c_{pv} q_t}\right), \tag{3}$$

$$\gamma \equiv \left(\frac{R_v q_t}{c_p + c_{pv} q_t}\right), \tag{4}$$

q_v is the water vapor mixing ratio, q_{snow} is the snow aggregate mixing ratio, q_{ice} is the cloud-ice mixing ratio, $q_i = q_{\text{snow}} + q_{\text{ice}}$, $q_t = q_v + q_{\text{snow}} + q_{\text{ice}}$ (all mixing ratios are in kg kg^{-1}), L_s is the latent heat of sublimation (J kg^{-1}), T is the temperature (K), c_p is the specific heat at constant pressure and c_{pv} is the specific heat at constant pressure over vapor (both in J kg^{-1} K^{-1}), T_v is the virtual temperature (K), R_d is the gas constant for

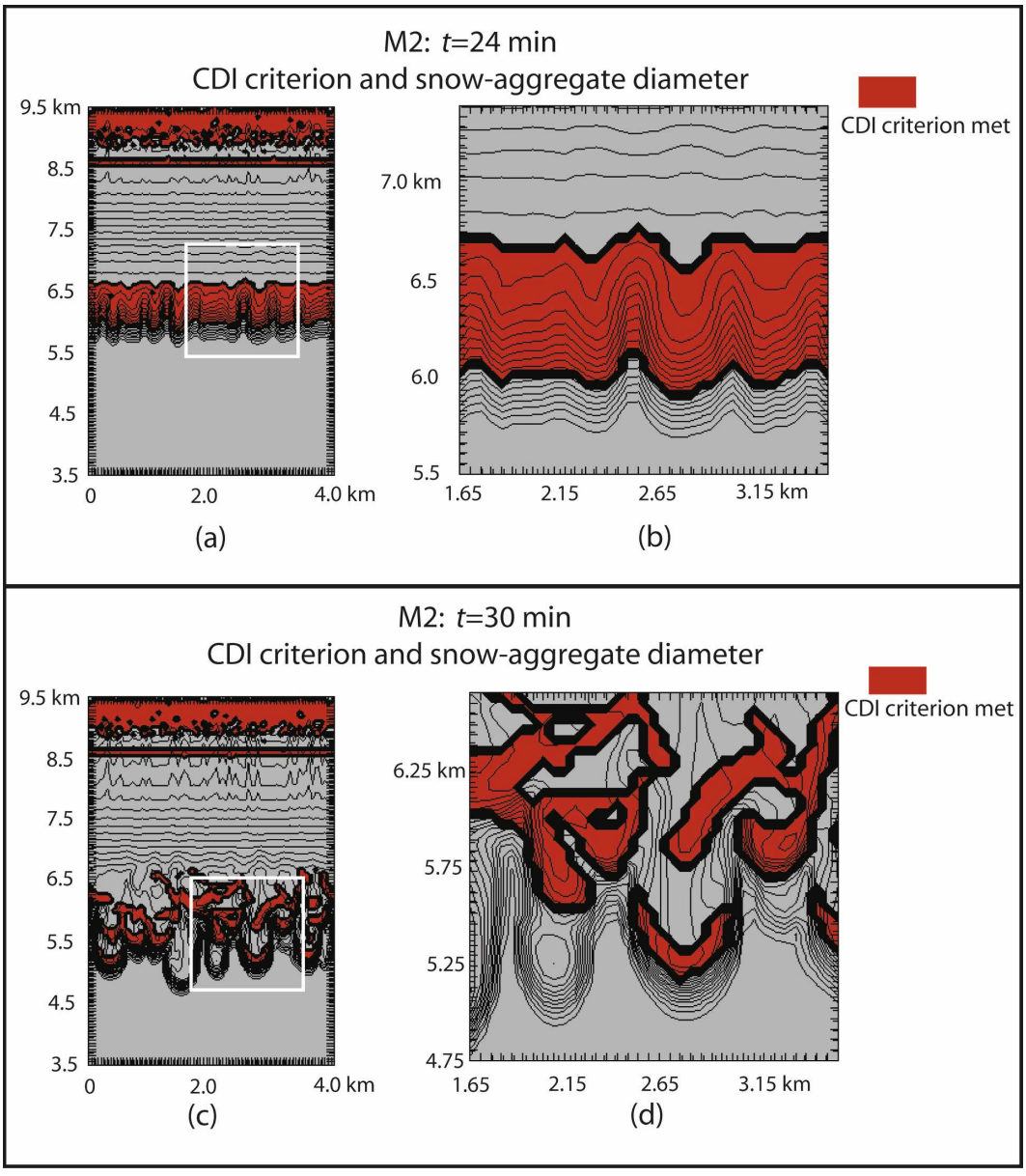

FIG. 6. Vertical cross sections at $y = 75$ m of the CDI criterion (red defines regions where ice-water static energy decreases with height) and snow aggregate diameter (mm, black lines) for M2: (a) whole domain at $t = 24$ min; (b) inset, white box in (a) indicates inset in (b); (c) whole domain at $t = 30$ min; (d) inset, white box in (c) indicates inset in (d).

dry air (J kg^{-1} K^{-1}), R_v is the gas constant for moist air (J kg^{-1} K^{-1}), p_o is the reference pressure (10^5 Pa), and p is the pressure (Pa). Thus, the CDI criterion is expressed as

$$\frac{\Delta\theta_{iv}}{\Delta z} < 0. \tag{5}$$

Equation (5) is evaluated everywhere throughout the model domain for M2 and at two times (24 min, a time near initial mammatus development, and 30 min, after mammatus are fully developed; Fig. 6). Equation (5) is satisfied all along the cloud base at 24 min (Figs. 6a,b), although by 30 min the region where (5) is satisfied has broken up (Figs. 6c,d). Locally, (5) is also satisfied within the middle of some lobes (Figs. 6c,d).

To determine if CDI was the distinguishing factor for the production of mammatus, (5) was also evaluated for N1 at 20 and 40 min (Fig. 7). Although (5) is satisfied all

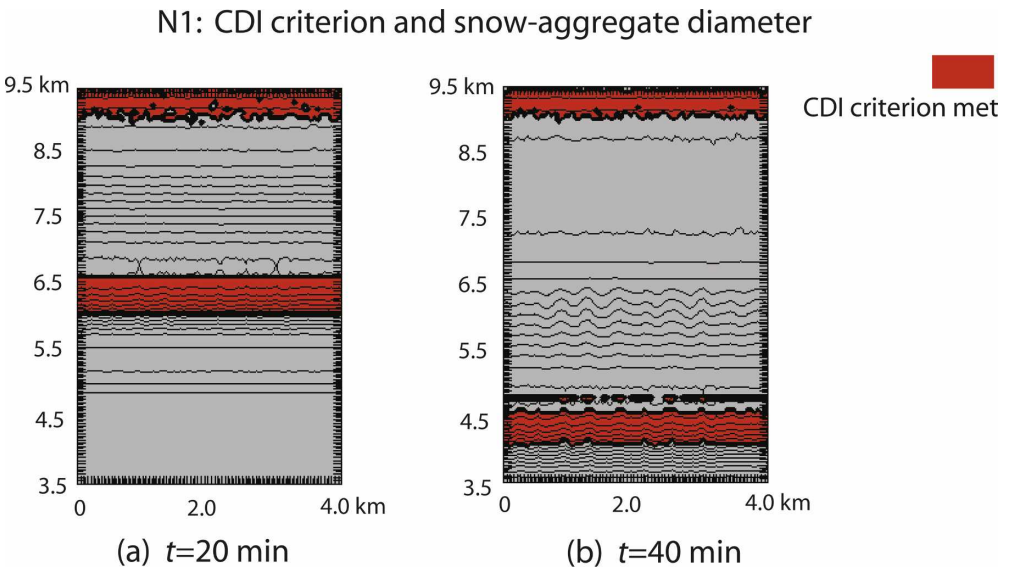

FIG. 7. Vertical cross sections at $y = 675$ m of the CDI criterion (red defines region where ice-water static energy decreases with height) and snow aggregate diameter (mm, black lines) for N1 at (a) $t = 20$ min and (b) $t = 40$ min.

along the cloud base at 24 min (Fig. 7a), the layer where (5) is satisfied simply descends with the cloud layer and is never deformed (Fig. 7b). No mammatus form at any time in N1. Thus, the satisfaction of the CDI criterion does not guarantee mammatus formation.

As a side experiment (not shown), a case where the CDI criterion was not initially met and hydrometeors had nonzero terminal velocity showed that falling hydrometeors can change the lapse rates across cloud base and thus the ice static energy, which results in the satisfaction of (5) and the formation of mammatus. On the other hand, for two simulations (not shown) that possess no regions satisfying (5) and the hydrometeors have zero terminal velocity, mammatus do not form. Consequently, for the small set of parameters considered here, satisfaction of the CDI criterion is a necessary, but not sufficient, condition for the formation of mammatus.

b. *Test of the hydrometeor fallout mechanism*

Simulation M2-NOFALL is designed to assess the relative importance of the hydrometeor fallout mechanism to the formation of mammatus. In this case, the fallout of hydrometeors process was "turned off" by setting the terminal velocity of the hydrometeors to zero. The hydrometeors still retained their mass and contributed to the hydrometeor loading, however. In the hydrometeor fallout mechanism for mammatus formation, precipitation particles are introduced into the dry subcloud layer by vertical flux. [This differs from CDI in which hydrometeors are introduced into a dry subcloud layer by spontaneous mixing under condition (5).]

Simulation M2-NOFALL shows that lobed structures occur, but are more isotropic in shape (Fig. 8) compared to the other cases M1–M4. The lobes are confined to the upper part of the simulation domain and are not distinctly separated from one another (Fig. 8a) as in the other cases. The expanded view in Fig. 8b shows that the lobes are about 300–400 m in horizontal extent.

c. *Test of the sublimation mechanism*

M2-NOSUBL is a simulation in which the sublimation process is turned off by setting the latent heat of sublimation to zero. In this case, no mammatus form by 30 min into the simulation (Figs. 8c,d). These results appear qualitatively similar to case N1 in which no mammatus lobes form (not shown). Thus, sublimation appears to be a required process for mammatus to exist. The results of simulations M2-NOFALL and M2-NOSUBL are consistent with Kanak and Straka (2006, their Fig. 4) who showed that sublimation dominated both hydrometeor loading and the effect of water vapor in the expression for buoyancy in simulation M2.

5. Sensitivity tests

The simulations in this paper suggest that the structure of the mammatus and intensity of vertical motions within the mammatus may depend on both the initial hydrometeor content and the ambient subcloud tem-

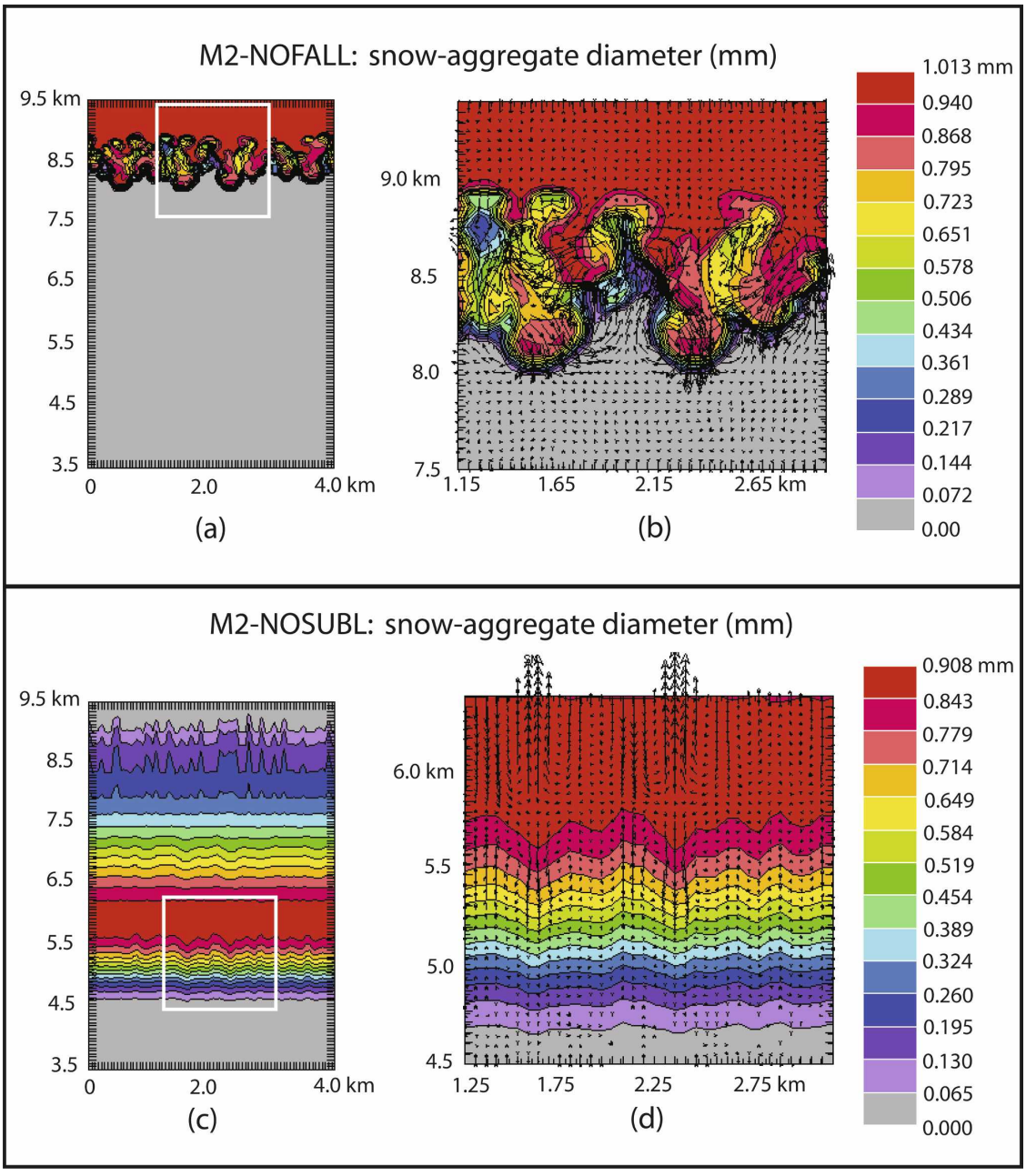

FIG. 8. Vertical cross sections of snow aggregate diameter (mm, color contours). (a) M2-NOFALL: whole domain at $y = 3725$ m and $t = 25$ min. (b) M2-NOFALL: inset with velocity vectors in black; white box in (a) indicates inset in (b). The longest vector corresponds to a wind speed of 0.62 m s^{-1}. (c) M2-NOSUBL: whole domain at $y = 3425$ m and $t = 30$ min. (d) M2-NOSUBL: inset with velocity vectors in black; white box in (c) indicates inset in (d). The longest vector corresponds to a wind speed of 0.19 m s^{-1}.

perature and moisture profiles. To examine the effects of the ambient environment, a series of idealized model simulations are initialized with soundings that emulate observed soundings associated with mammatus. These simulations test the sensitivity of the mammatus to changes in the subcloud static stability in section 5a and subcloud relative humidity in section 5b.

a. Sensitivity of mammatus to the subcloud static stability

One primary similarity between the four observed mammatus soundings M1–M4 is the dry-adiabatic subcloud layer. To examine the importance of this dry-adiabatic subcloud layer to the existence of the mam-

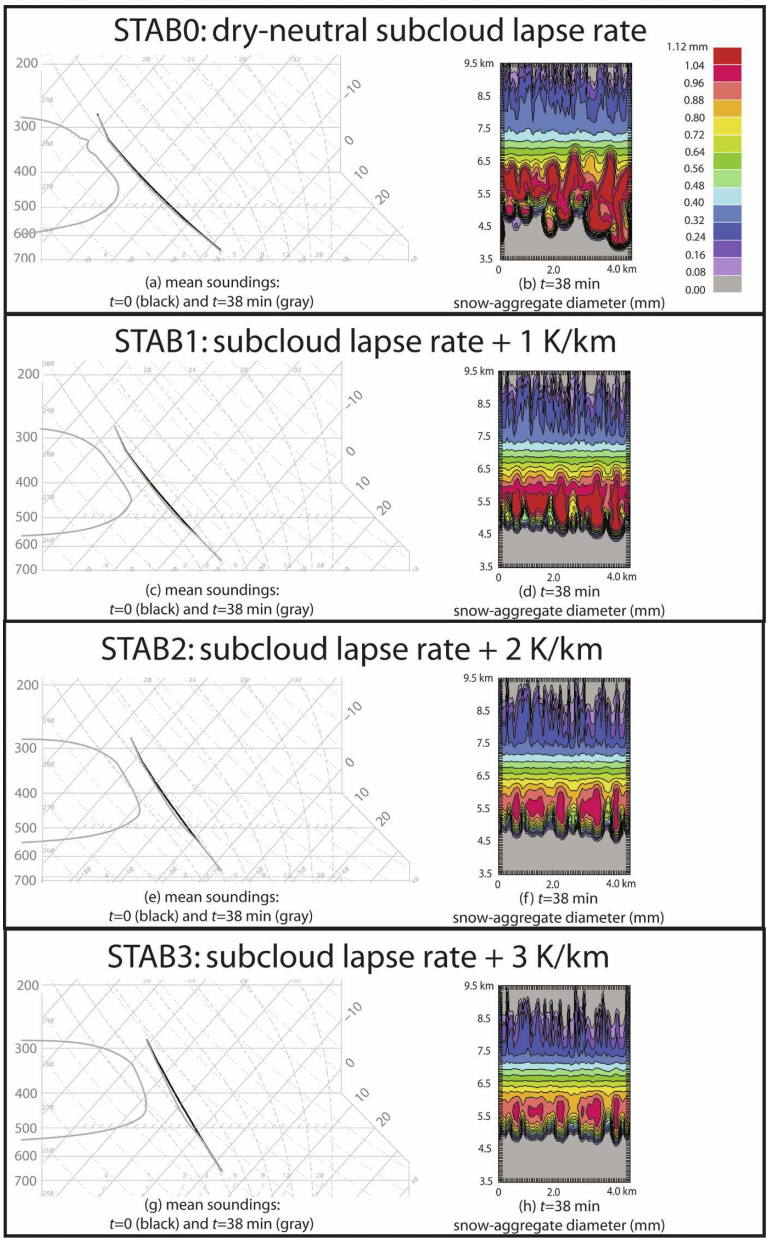

FIG. 9. Simulations in which subcloud static stability is varied. Idealized soundings (black lines) used to initialize the simulations and model-generated soundings at $t = 38$ min (gray lines). Dewpoint (lhs lines) and temperature (rhs lines) are plotted for (a) STAB0: dry neutral lapse rate, (c) STAB1: dry neutral lapse rate +1 K km^{-1}, (e) STAB2: dry neutral lapse rate +2 K km^{-1}, and (g) STAB3: dry neutral lapse rate +3 K km^{-1}. Vertical cross sections at $y = 725$ m and $t = 38$ min of snow aggregate diameter (mm, color contours) for (b) STAB0, (d) STAB1, (f) STAB2, and (h) STAB3.

matus, artificial thermodynamic profiles representing the observed soundings are constructed. Simulation STAB0 is initialized with a dry-adiabatic lapse rate (9.8°C km^{-1}) from 3500 to 7500 m and a lapse rate in the cloud of 3°C km^{-1} above 7500 m (Fig. 9a). The initial relative humidity is set to 90% with respect to ice inside the cloud and 10% below the cloud base. Three subsequent simulations are characterized by initial subcloud temperature distributions that are increasingly more stable, as the temperature lapse rate between

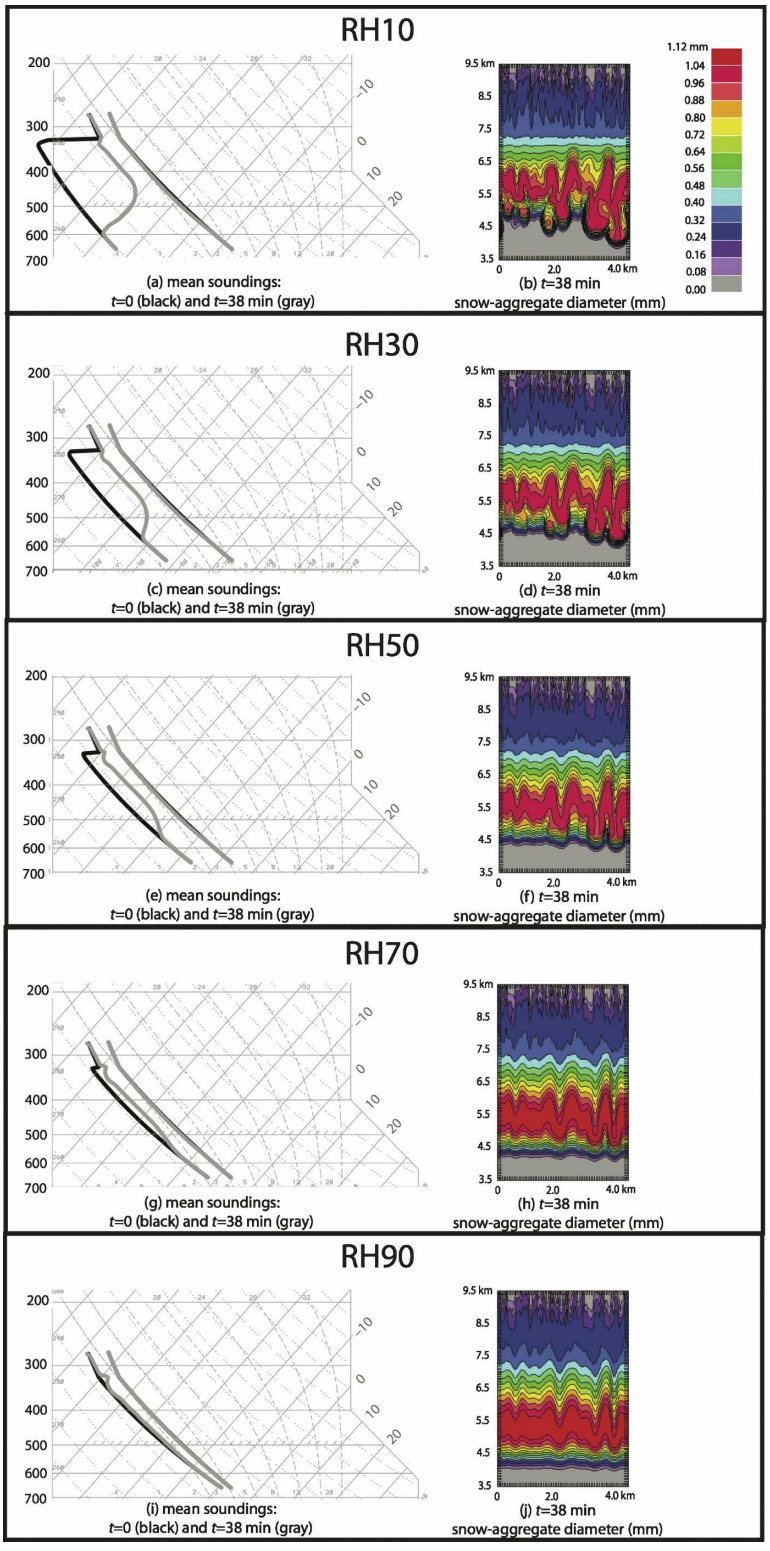

FIG. 10. Simulations in which subcloud relative humidity is varied using idealized soundings (black lines) to initialize the simulations and model-generated soundings at $t = 38$ min (gray lines). Dewpoint (lhs lines) and temperature (rhs lines) are plotted for (a) RH10: 10% RH; (c) RH30: 30% RH; (e) RH50: 50% RH; (g) RH70: 70% RH; and (i) RH90: 90% RH. Vertical cross sections at $y = 725$ and $t = 38$ min of snow aggregate diameter (mm, color contours) for (b) RH10, (d) RH30, (f) RH50, (h) RH70, and (j) RH90.

3500 and 7500 m is stabilized by 1°C km^{-1} for STAB1 (8.8°C km^{-1}, Fig. 9c), 2°C km^{-1} for STAB2 (7.8°C km^{-1}, Fig. 9e), and 3°C km^{-1} for STAB3 (6.8°C km^{-1}, Fig. 9g).

Mammatus lobes in STAB0 are well developed and distinct from each other (Fig. 9b) in the subcloud layer with dry-adiabatic lapse rate (Fig. 9a). After 38 min, these lobes have descended as low as 3.7 km (Fig. 9b). Increasing the static stability in STAB1, STAB2, and STAB3 produces mammatus lobes that are smaller and less separated from each other (Figs. 9d,f,h). In addition, simulations with the higher subcloud static stability produce lobes that do not descend as far as in STAB0 (cf. Figs 9d,f,h and 9b). Specifically, mammatus in STAB1 descend to a height of about 4.5 km by 38 min (Fig. 9d), whereas, for STAB2 and STAB3, the mammatus extend to just above 4.5 km (Figs. 9f,h). Thus, even relatively low subcloud stability (6.8°–7.8°C km^{-1}) inhibits the development of rounded and well-developed mammatus lobes for the parameters considered. This series of simulations supports the earlier results from M1–M4 indicating that subcloud layers characterized by lapse rates that are less stable appear to favor the formation of deep, well-developed mammatus lobes.

b. *Sensitivity of mammatus to subcloud relative humidity*

To test the sensitivity of the mammatus to the subcloud relative humidity, the STAB0 sounding is modified by incrementally increasing the subcloud relative humidity from 10% to 30%, 50%, 70%, and 90% in simulations RH10 (same as STAB0) to RH30, RH50, RH70, and RH90 (Figs. 10a,c,e,g,i).

As previously shown in STAB0 (Fig. 9b), the mammatus lobes at 38 min in RH10 develop deep vertical structure, extending down to about 3.7 km with a horizontal extent of 500 m (Fig. 10b). For RH30 (Fig. 10d), fewer distinct lobes exist and they penetrate slightly less than in RH10. For RH50 (Fig. 10f), the mammatus lobes are smaller in vertical depth and are almost indistinguishable from one another. For RH70 and RH90 (Figs. 10h,j), the cloud base merely features undulations, not mammatus. For this idealized temperature profile, cloud microphysical properties, and the formulation of the simulations, an estimated value of subcloud relative humidity greater than which no mammatus can form is about 50%.

Another effect of the subcloud relative humidity is on the depth to which the cloud deck descends due to the falling hydrometeors. As the subcloud relative humidity is increased from 10% to 90% in these simulations, the snow aggregate diameter has maxima at only slightly lower altitudes than cases with lower relative humidity (Fig. 10). In contrast, increasing the subcloud static stability resulted in comparatively higher cloud heights (Fig. 9). Thus, the static stability has a greater inhibiting effect on the descent of the cloud deck than does the subcloud relative humidity.

The subcloud thermodynamic profiles (Figs. 10a,c,e,g,i) show moistening and cooling, consistent with sublimation in the descending lobes. Indeed, all of the soundings show this same behavior, but the effect is most dramatic for the simulations with the lower values of relative humidity. Thus, even for the cases without mammatus (e.g., Figs. 10g–j), the subcloud thermodynamic profiles are modified in the same manner: moistened and cooled. Therefore, this cooling and moistening could be related to cloud-base processes associated with any subcloud layer, depending on the thermodynamic profile and the hydrometeor composition of the cloud, whether or not mammatus form.

Emanuel (1981) argued that too much subcloud moisture would preclude the evaporative/sublimative cooling that mammatus need to descend, whereas too little subcloud moisture would evaporate/sublimate all the hydrometeors in the mammatus lobes so quickly as to inhibit their formation. The model simulations in the present paper support Emanuel's (1981) former statement, but not his latter, because the driest subcloud air favors the most well-developed mammatus. Our model simulations, however, have an abundant supply of hydrometeors. Simulations with a more limited hydrometeor supply may produce results more in agreement with Emanuel's (1981) statements, which is a hypothesis that remains to be tested.

6. Conclusions

This study demonstrated that mammatus can be simulated using a three-dimensional, high-resolution, numerical model starting from realistic, thermodynamically horizontally homogeneous, initial conditions. Observed soundings close in time and space to visual observations of mammatus associated with cumulonimbus cirrus anvils were used to initialize the simulations. The simulated mammatus exhibited rounded, pouchlike protuberances at the base of a layer of cloud ice and snow aggregates with physical dimensions and vertical motions comparable to previously published observations of mammatus. In addition, one simulation was performed of an anvil associated with no visual observations of mammatus; this simulation did not produce mammatus.

The four observed soundings associated with mam-

matus had dry subcloud layers below moist-adiabatic cloud layers. The dry subcloud layer was not present in the one sounding not associated with observed mammatus. Simulations with observed mammatus soundings showed that the horizontal extent and potential temperature perturbations of the lobes were dependent on the ambient sounding.

The descent of the mammatus-laden cloud deck resulted in cooling and moistening of the initial sounding. The simulations also explain the apparent contradictory observations of subcloud inversions and superadiabatic layers in association with mammatus. Late stages in the simulations showed different inhibited descent of the mammatus and the breaking away of some cloud portions.

Three possible mechanisms for mammatus formation were evaluated: cloud-base detrainment instability, hydrometeor fallout, and sublimation of hydrometeors. Radiative effects and vertical shear of the horizontal wind were not tested in the experiments described in this paper.

The first mechanism tested was CDI. Simulations in which the CDI criterion was not satisfied did not produce mammatus; however, not all simulations with CDI produced mammatus. Consequently, for the parameters considered, satisfaction of the CDI criterion appears to be a necessary, but not sufficient, condition for the formation of mammatus. The second mechanism tested was the fallout of hydrometeors. When fallout was not allowed to occur, the character of these lobes was more rounded and confined to the upper part of the domain as compared with the other simulations. The third mechanism tested was sublimation. No mammatus formed when sublimation was not allowed to occur. These results support those of Kanak and Straka (2006), who found that the cooling due to sublimation was the largest term producing negative buoyancy in the mammatus.

Increased ambient subcloud static stability resulted in reduced horizontal size and vertical penetration of the mammatus. Increased subcloud relative humidity resulted in a similar effect. One difference was that changes in the static stability had a greater inhibiting effect on the descent of the cloud deck than did changes in the subcloud relative humidity. At subcloud relative humidity around 50%, mammatus formation was essentially inhibited.

The simulations show that the shape, scale, and evolution of the simulated mammatus depend on several environmental parameters, including subcloud moisture and stability profiles and the terminal velocities of the hydrometeors in the mammatus. Although a small region of the possible phase space was examined with the experiments in this paper, further numerical experimentation can yield further insight into the dynamics and microphysics of mammatus. Furthermore, the inability of the CDI criterion to completely and quantitatively predict the occurrence of mammatus indicates that a more comprehensive theory awaits formulation.

Acknowledgments. We are grateful to Professor Kerry Emanuel for many helpful suggestions and discussions. We also thank two anonymous reviewers for their comments. Partial funding for Kanak and Schultz was provided by NOAA/Office of Oceanic and Atmospheric Research under NOAA–University of Oklahoma Cooperative Agreement NA17RJ1227, Department of Commerce. This work was also supported by National Science Foundation Grants ATM-0339519, ATM-0340639, ATM-0446509, and ATM-0646892.

REFERENCES

Berg, H., 1938: Mammatus developments (in German). *Meteor. Z.,* **55,** 283–287.

Carpenter, R. L., Jr., K. K. Droegemeier, and A. M. Blyth, 1998: Entrainment and detrainment in numerically simulated cumulus congestus clouds. Part I: General results. *J. Atmos. Sci.,* **55,** 3417–3432.

Clarke, R. H., 1962: Pressure oscillations and fallout downdraughts. *Quart. J. Roy. Meteor. Soc.,* **88,** 459–469.

Clayton, H. H., 1911: A study of clouds with data from kites. *Ann. Astron. Observatory Harvard Coll.,* **68,** 170–192.

Deardorff, J. W., 1980: Stratocumulus-capped mixed layers derived from a three-dimensional model. *Bound.-Layer Meteor.,* **18,** 495–527.

Emanuel, K. A., 1981: A similarity theory for unsaturated downdrafts within clouds. *J. Atmos. Sci.,* **38,** 1541–1557.

——, 1994: *Atmospheric Convection.* Oxford University Press, 580 pp.

Glickman, T. S., Ed., 2000: *Glossary of Meteorology.* 2nd ed. Amer. Meteor. Soc., 855 pp.

Hartmann, W., 1920: About the origin of mammatus forms (in German). *Meteor. Z.,* **37,** 216–220.

Heymsfield, A. J., 1986: Ice particle evolution in the anvil of a severe thunderstorm during CCOPE. *J. Atmos. Sci.,* **43,** 2463–2478.

——, and R. G. Knollenberg, 1972: Properties of cirrus generating cells. *J. Atmos. Sci.,* **29,** 1358–1366.

Kanak, K. M., and J. M. Straka, 2006: An idealized numerical simulation of mammatus-like clouds. *Atmos. Sci. Lett.,* **7,** 2–8.

Kollias, P., I. Jo, and B. A. Albrecht, 2005: High-resolution observations of mammatus in tropical anvils. *Mon. Wea. Rev.,* **133,** 2105–2112.

Leonard, B. P., 1991: The ULTIMATE conservative difference scheme applied to unsteady one-dimensional advection. *Comput. Methods Appl. Mech. Eng.,* **88,** 17–74.

Martner, B. E., 1995: Doppler radar observations of mammatus. *Mon. Wea. Rev.,* **123,** 3115–3121.

Sassen, K., J. M. Comstock, Z. Wang, and G. G. Mace, 2001: Cloud and aerosol research capabilities at FARS: The Facil-

ity for Atmospheric Remote Sensing. *Bull. Amer. Meteor. Soc.,* **82,** 1119–1138.

Schneider, K., 1920: The inversion at the base of stratus mammatus (in German). *Meteor. Z.,* **37,** 137–139.

Schultz, D. M., and Coauthors, 2006: The mysteries of mammatus clouds: Observations and formation mechanisms. *J. Atmos. Sci.,* **63,** 2409–2435.

Stith, J. L., 1995: In situ measurements and observations of cumulonimbus mamma. *Mon. Wea. Rev.,* **123,** 907–914.

Straka, J. M., and J. R. Anderson, 1993: Extension and application of a local, minimum aliasing method to multidimensional problems in limited-area domains. *Mon. Wea. Rev.,* **121,** 2903–2918.

——, and E. R. Mansell, 2005: A bulk microphysics parameterization with multiple ice precipitation categories. *J. Appl. Meteor.,* **44,** 445–466.

Tremback, C. J., J. Powell, W. R. Cotton, and R. A. Pielke, 1987: The forward-in-time upstream advection scheme: Extension to higher orders. *Mon. Wea. Rev.,* **115,** 540–555.

Wang, L., and K. Sassen, 2006: Cirrus mammatus properties derived from an extended remote sensing dataset. *J. Atmos. Sci.,* **63,** 712–725.

Warner, C., 1973: Measurements of mamma. *Weather,* **28,** 394–397.

Winstead, N. S., J. Verlinde, S. T. Arthur, F. Jaskiewicz, M. Jensen, N. Miles, and D. Nicosia, 2001: High-resolution airborne radar observations of mammatus. *Mon. Wea. Rev.,* **129,** 159–166.